Journal of Materials Chemistry A

Accepted Manuscript

ROYAL SOCIETY OF CHEMISTRY

www.rsc.org/materialsA

Three-dimensional Mn-doped Zn_2GeO_4 nanosheet array hierarchical nanostructures anchored on porous Ni foam as binder-free and carbon-free lithium-ion battery anodes with enhanced electrochemical performance

Qun Li[a,b], Xianguang Miao, Chengxiang Wang and Longwei Yin[a]*

[a]Key Laboratory for Liquid-Solid Structural Evolution and Processing of Materials, Ministry of Education, School of Materials Science and Engineering, Shandong University, Jinan 250061, P. R. China

[b]College of Chemistry and Chemical Engineering, Taishan University, Tai'an 271021, P. R. China

Email: yinlw@sdu.edu.cn

ABSTRACT We report on three dimensional Mn-doped Zn_2GeO_4 hierarchical nanosheet arrays anchored on porous Ni foam as binder-free lithium-ion battery (LIB) anodes with enhanced electrochemical performance. Homogeneously Mn doping effectively induces a great microstructure evolution from nanowire array for pure Zn_2GeO_4 to nanosheet array for Mn-doped Zn_2GeO_4 samples. The LIBs anodes based on 7%Mn-Zn_2GeO_4 nanosheet array hierarchical nanostructures anchored Ni foam display significantly improved electrochemical Li storage performance, showing a superior reversible capacity of 1301 mA h g^{-1} at a current density of 100 mA g^{-1} after 100 cycles, almost two times higher than that of 660 mA h g^{-1} for pure Zn_2GeO_4 sample. An extraordinarily excellent rate capability with a capacity of 500 mA h g^{-1} at a current density of 2 A g^{-1} can be obtained for LIBs anodes based on Mn-doped Zn_2GeO_4 hierarchical nanostructures. The great enhancement of the electrochemical lithium storage performance can be attributed to three-dimensional interconnected conductive channels composed of the Ni foam, which not only serves as the current collector but also buffers the volume change of the active material upon cycling. Additionally, the Mn doping can greatly improve charge transport kinetics at the interface between the electrode and electrolyte.

KEYWORDS：Zinc germinate; doping; microstructure; lithium ion battery; anode material

1. Introduction

Lithium-ion batteries (LIBs) have been widely utilized in portable electronic devices, electric vehicles and power tools, because of their high energy density, high rate capability, high safety and low cost.[1,2] However, current LIBs anode materials based on graphite are limited by its low theoretical specific capacity of 372 mA h g^{-1}. Much attention has been paid to the development of new anode materials with high capacity and good cycling performance, such as transition metal oxide,[3-5] silicon (Si),[6] germanium (Ge)[7-11] and tin (Sn)[12] et al. Compared with Si, Ge displays several advantages for high-power LIBs because of its intrinsic kinetic superiority.[8-10] For instance, Ge has a four order of magnitude higher electronic conductivity and hundreds of times higher Li-ion diffusion coefficient than Si.[10] Recently, ternary metal (Zn,[13-18] Ca,[19-21] Fe,[22] Cu,[23] Co[24,25]) germanate nanostructures with a high specific capacity are attracting attention as high-performance LIBs anodes. Unfortunately, until now, the rational design on tunable microstructure and chemical composition, and thereby electrochemical performance of germanate nanostructures with high specific capacity and perfect cycling stability performance is of great challenge and fundamental importance.

Zn_2GeO_4, has attracted much attention due to its unique optical, electronic, catalytic properties.[26-30] It can also be considered as an ideal candidate for high-performance LIBs anode materials because of its high capacity, low voltage and non-poisonousness. Theoretically, the lithium storage mechanism for Zn_2GeO_4 can be described as follows:

$$Zn_2GeO_4 + 8\ Li^+ + 8\ e^- \rightarrow 2\ Zn + Ge + 4\ Li_2O \quad (1)$$

$$Ge + 4.4\ Li^+ + 4.4e^- \longleftrightarrow Li_{4.4}Ge \quad (2)$$

$$2Zn + 2Li^+ + 2e^- \longleftrightarrow 2LiZn \quad (3)$$

$$2Zn + 2Li_2O \longleftrightarrow 2ZnO + 4Li^+ + 4e^- \quad (4)$$

$$Ge + 2Li_2O \longleftrightarrow GeO_2 + 4Li^+ + 4e^- \quad (5)$$

The lithium storage mechanism of Zn_2GeO_4 anode is described by the initial conversion reaction and followed by the alloying reactions. In the first cathodic process, Zn_2GeO_4 can be reduced into Zn, Ge and Li_2O firstly. This chemical reduction process is irreversible, as shown in Eq. 1. Then, the metal Zn and Ge can uptake Li^+ and form LiZn and $Li_{4.4}Ge$ alloy. During the anodic process, LiZn and $Li_{4.4}Ge$ alloy will transform to metal Zn, Ge and release Li^+, corresponding to Eq. 2 and 3. The reversible capacity is believed to be only 644 mA h g^{-1} based on Eq. 1 - 3.[8] However, metal Zn and Ge obtained from the anodic process can be re-oxided to ZnO and GeO_2 with Li_2O, corresponding to Eq. 4 and 5. Considering these chemical actions, 1 mole Zn_2GeO_4 anode material can uptake and release 14.4 mole electrons, corresponding to a theoretical reversible capacity of 1450 mA h g^{-1}.[8,13] Actually, Li_2O formed during the first lithiation is irreversible to a great extent, meaning that the lithium storage process can be

mainly described by Eq. 1 - 3.[13-15] It may cause a large initial irreversibly capacity and low initial coulombic efficiency. Combining with carbonaceous materials, such as graphene, is the major strategy to overcome the obstacles for improving the electrochemical performance of Zn_2GeO_4. Zou et al.[13] prepared the sandwiched Zn_2GeO_4-graphene oxide nanocomposite, showing a high initial coulombic efficiency of 60% (only 35% for pure Zn_2GeO_4 nanorods) and a specific capacity of 1150 mA h g^{-1}. It is believed that the highly reversible capacity and excellent rate capability arise from synergetic chemical coupling effects between Zn_2GeO_4 and graphene oxide. The partially crystalline Zn_2GeO_4 nanorod/graphene composites prepared by Wang et al.[16] demonstrates a specific capacity of 768 mA h g^{-1} after 50 cycles. It should be noted that the synthetic process for graphene-based composites in a large scale, is always tedious and expensive.

Particularly, cationic doping has been considered as another effective strategy to improve electrical conductivity and charge transfer ability and thus enhance the electrochemical performance of metal oxide anode materials.[31-36] Up to now, different metal cations have been incorporated into lattice of variety of metal oxides to improve the electrochemical performance. For instance, Cu cation doping can increase the specific capacity from 361 mA h g^{-1} of Mn_2O_3 to 642 mA h g^{-1} for Cu-doped Mn_2O_3.[5] Zou's study demonstrates that Mn-doped V_2O_5 sheet can display a specific capacity of 600 mA h g^{-1}, which is two times higher than that of pure V_2O_5 sheet sample.[34] Recently, it is reported that Co doping in Zn_2SnO_4 can greatly enhance the cycle stability and rate capability.[35]

On the other hand, most of the conventional LIBs anodes usually use polymer and carbon black as binders, which may experience virtually swelling in commonly used electrolytes, leading to a rapid capacity degradation, poor cycle stability and rate capability.[31] The polymer and carbon black additives generate a weight increase (10-40%) for the battery electrode and extra steps to mix and combine those materials into a film form. It is difficult to obtain a homogeneous blend of carbon black, binders, and active electrode materials. Also, the diffusion path of the ions and electrons is unclear, and it is not easy to model and characterize. To solve this obstacle, a new concept is brought forward to grow active materials on conductive substrates, such as porous and conductive foam Ni, as binder-free and carbon-free electrodes for LIBs and supercapacitor.[4,15,32,33] Such a kind of binder-free electrode could provide fast electron-transport access to the current collector, the conductive substrate can serve as a highway to transport electron fast access to the active material, efficiently reduce ohmic polarization, leading to a high rate capability and better cyclic stability. Up to now, it is of great challenging and of great importance to tune hierarchically microstructure and effectively realize cationic doping to improve the electrochemical performance of binder-free and carbon-free Zn_2GeO_4 LIBs anode materials.

Herein, we rationally designed a facile route to synthesize three dimensional Mn-doped Zn_2GeO_4 nanosheet array hierarchical nanostructrues anchored Ni foam as a binder-free electrode for LIBs. The incorporation of Mn

into lattice of Zn_2GeO_4 induces a great microstructure evolution from nanowire array for pure Zn_2GeO_4 to nanosheet array for Mn-doped Zn_2GeO_4 sample. The microstructure and electrochemical performance of Mn-doped Zn_2GeO_4 can be tuned by controlling the Mn doping concentration. The Mn doping induced three-dimensional Mn-Zn_2GeO_4 nanosheet array hierarchical nanostructures anchored on Ni foam display superior electrochemical performance as binder-free LIBs anodes, exhibiting a highly reversible capacity of 1301 mA h g^{-1} at a current density of 100 mA g^{-1} after 100 cycles, and excellent rate capability with a capacity of as high as 500 mA h g^{-1} even at 2.0 A g^{-1}.

2. Experimental Section

2.1 Material Synthesis

All chemical reagents are analytical grade without further purification, from Shanghai Chemical Co. Ltd. China. In a typical synthesis, 0.3 g GeO_2, 0.825 g $Zn(CH_3COO)_2{\cdot}2H_2O$ were added into a mixture of 32 mL diethylenetriamine (DETA) and 8 ml H_2O under stirring. The resultant mixture was continually stirred for 1 h to obtain a homogeneous solution and then transferred into a 50 mL teflon-lined stainless-steel autoclave. A piece of Ni foam was put into the autoclave vertically. Teflon-lined autoclave was put into an oven at 180 °C for 48 h. The system was then cooled to ambient temperature naturally. The Zn_2GeO_4 sample grown on the Ni foam was washed with distilled water and absolute alcohol at least five times and dried in an oven at 60 °C, which was designated as Zn_2GeO_4 sample. The Mn doped Zn_2GeO_4 samples on Ni foam with different Mn doping concentrations (3 at%, 5 at%, 7 at% and 9 at%) synthesized using $Mn(CH_3COO)_2{\cdot}4H_2O$ as a Mn source, are designated as 3%Mn-Zn_2GeO_4, 5%Mn-Zn_2GeO_4,7%Mn-Zn_2GeO_4 and 9%Mn-Zn_2GeO_4 samples, respectively.

2.2 Structure Characterization

The crystal structure of the samples was characterized by powder X-ray diffraction (XRD) patterns (Rigaku D/Max-KA diffractometer, Cu Ka radiation). X-ray photoelectron spectroscopy (XPS) characterization was carried out in an ESCALAB 250 instrument with 150 W Al Ka probe beam. The morphology and microstructure of the as-prepared samples were characterized by SU-70 field emission scanning electron microscopy (FESEM) and high-resolution transmission electron microscopy (HRTEM) of JEM-2100 at an acceleration voltage of 200 kV. The chemical components of the products were measured with an energy dispersive X-ray energy dispersive spectrometer (EDS).

2.3 Electrochemical Characterization

The electrochemical measurements were conducted using standard 2025 type coin cells with Zn_2GeO_4 grown on Ni foam as working electrode, lithium foil as reference electrodes and 1.0 M $LiPF_6$ in mixed ethylene

carbonate (EC) and diethyl carbonate (DEC) (EC:DEC, 1:1 by volume) as the electrolyte. A cutoff voltage window of 0.01-2.0 V was used. The 2025 coin-type cells were galvanostatically cycled on a LAND CT2001A instrument (Wuhan, China) at room temperature. Cyclic voltammetry study was conducted in a PARSTAT2273 electrochemical workstation between 0.01-3.0 V at a scan rate of 0.1 mV s^{-1}. Electrochemical impedance spectroscopy (EIS) measurements were performed in the frequency between 100 kHz and 10 mHz and the amplitude is 5 mV. Both the Ni foam combined with active material and bare Ni foam were weighed by a high-precision analytical balance. We weighed ten different electrodes and then got the average value. The reading differences are the exact mass of the active materials grown on the Ni foam. The mass loading of active material for Zn_2GeO_4 sample and Mn doped Zn_2GeO_4 sample is about 1.38 mg cm^{-2} and 1.05 mg cm^{-2} in average, respectively. The present loading density of the active material on the electrode is higher than that of other binder free electrode, for example, NiO anchored Ni[4] and $MnMoO_4 \cdot 4H_2O$ nanoplates grown on a Ni foam[32].

3. Results and discussion

The crystal structure of pure Zn_2GeO_4 and Mn-doped Zn_2GeO_4 samples are studied by X-ray diffraction pattern (XRD). Fig. 1a shows the XRD pattern of Zn_2GeO_4 sample obtained via a solvothermal reaction route. All the diffraction peaks can be indexed to the rhombohedral phase of Zn_2GeO_4 (JCPDS No. 11-0687). The XRD pattern of the 7%Mn-Zn_2GeO_4 sample shown in Fig. 1b is basically in agreement with that of rhombohedral Zn_2GeO_4, except for that the intensity of the diffraction peaks becomes weaker compared with that of pure Zn_2GeO_4. Furthermore, the diffraction peaks shift left to the positions at small angles, indicating that the incorporation of Mn into lattice of Zn_2GeO_4 results in the increase of lattice constant of Zn_2GeO_4. Fig. 1c-1d depicts the XRD patterns of magnified (220) and (410) peaks of Zn_2GeO_4 and 7%Mn-Zn_2GeO_4 sample, clearly showing that (220) and (410) peaks shift to positions at smaller angles. The reason for the lattice expansion of Mn-doped Zn_2GeO_4 is due to a larger radius of Mn^{2+} (0.080 nm) than that of Zn^{2+} ion (0.072 nm).[37] The lattice parameters of pure Zn_2GeO_4 and Mn-doped Zn_2GeO_4 samples can be calculated using the Bragg equation, with lattice constants of a = 14.27442 Å, c = 9.54898 Å for pure Zn_2GeO_4, and lattice constants of a = 14.30313 Å, c = 9.56151 Å for 7%Mn-Zn_2GeO_4, respectively.

The chemical composition and chemically bonding state of 7%Mn-Zn_2GeO_4 sample are investigated by XPS analysis, as shown in Fig. 2. The overall XPS spectrum reveals that the as-obtained 7%Mn-Zn_2GeO_4 sample is composed of Zn, Ge, O, and Mn species (Fig. 2a). Fig. 2b depicts a high-resolution XPS spectrum of Ge 3d peak centered at 34.7 eV, corresponding to Ge-O bonding in the form of Ge^{4+} tetravalent.[11,13,21]. The peaks located at 1023 and 1046 eV in Fig. 2c, are attributed to Zn $2p_{3/2}$ and Zn $2p_{1/2}$, revealing the oxidation state of Zn^{2+}.[30] Fig. 2d

displays the high-resolution XPS spectrum of Mn 2p with two peaks centered at 641.6 and 653.2 eV, can be attributed to Mn $2p_{3/2}$ and Mn $2p_{1/2}$ levels, respectively. The spin energy separation is about 11.6 eV, which is a signature of the Mn^{2+} oxidation state.[38,39]

The morphologies of the synthesized Zn_2GeO_4 products are observed by field emission scanning electron microscopy (FE-SEM). Fig. 3 shows the FE-SEM images of pure Zn_2GeO_4 sample grown on Ni foam, showing the nanoflower structure characteristics assembled from Zn_2GO_4 nanowires with a length of 2-3 μm and diameter of 20-30 nm. It is interesting to note that Mn doping can effectively induce a great microstructure evolution from nanowire array for pure Zn_2GeO_4 to nanosheet array for Mn-doped Zn_2GeO_4 samples.

For the growth mechanism and the structure evolution of Mn doped Zn_2GeO_4 samples, the effect of doping level and solvothermal reaction time is investigated. We study the effect of the solvothermal action time on the microstructure evolution. Fig. S1 shows the morphology of the 7%Mn doped Zn_2GeO_4 sample obtained at different solvothermal action time of 12 h, 24 h and 48 h. It is clearly shown that the Mn doped Zn_2GeO_4 nanosheets grow gradually with the increase of the action time. As the reaction time is 12 h, the 7%Mn-doped Zn_2GeO_4 sample shows a small size for interconnected nanosheet arrays. When the action time increases to 24 h and 48 h, the Mn-doped Zn_2GeO_4 nanosheet arrays grow into interconnected 3D nanosheet array structures.

The effect of Mn doping level on the microstructure evolution and related process is also systematically investigated. It demonstrates that the microstructures of Mn-doped Zn_2GeO_4 samples can be tuned by adjusting the Mn doping level. The 1%Mn-Zn_2GO_4 sample anchored on 3D Ni foam only exhibits the morphology of nanoplate distributing arbitrarily on surface of porous Ni foam, significantly difference from that of the pure Zn_2GO_4 hierarchical nanorod array samples anchored on Ni foam, as shown in Fig. S2a-2b.

With the Mn doping content further increasing, the Mn-doped Zn_2GeO_4 nanaplates grow and self-assemble into the interconnected porous hierarchical framework nanostructures. As the Mn doping content increases to 3%, distinctively different from that of pure Zn_2GeO_4 and 1%Mn-Zn_2GeO_4 samples grown on Ni foam, the 3D hierarchical nanosheet array nanostructures of Mn-doped Zn_2GeO_4 are formed (Fig. 4a-4c), with the nanosheet arrays interconnected to form the 3D ordered architectures, even though the length of Zn_2GeO_4 nanosheets is not so large, relatively smaller than that of 7%Mn-Zn_2GeO_4.

With the Mn doping content increasing to 5%, the size for the length of 5%Mn-Zn_2GeO_4 nanosheet arrays gets larger, and the typical 3D hierarchical nanostructures are formed (Fig. 4d). Fig. 5a-5c depict typical low-magnification FESEM images of the 7%Mn-Zn_2GeO_4 3D nanostructures anchored on porous Ni foam, displaying 3D nanosheet array hierarchical nanostructures, with the nanosheet interconnected each other to form distinctly 3D opened-up hierarchical ordered networks. Fig. 5d gives a higher magnification FESEM image of

7%Mn-Zn_2GeO_4 hierarchical nanostructures, demonstrating the hierarchical nanostructures are assembled from uniform nanosheets, interconnecting each other to form the typical 3D ordered networks. The structures of Mn-doped Zn_2GeO_4 samples can be tuned by adjusting the Mn doping concentration. Fig. S2c-2d shows the SEM images of the 9%Mn-Zn_2GeO_4 sample, displaying the similar structure to that of 7%Mn-Zn_2GeO_4 sample. The cross-section SEM images of 7% Mn-Zn_2GeO_4 sample (Fig. S3) reveal that the thickness of the Mn doped Zn_2GeO_4 nanosheet film is about 1 μm, indicating a higher loading mass of the active material.[40] The cross-section SEM images of the nanosheet film also display a uniformly thickness, which demonstrates Mn doped Zn_2GeO_4 nanosheet samples with the uniform depth can be deposited on Ni foam.[40,41] The cross-section SEM images show that the depth of the Mn doped Zn_2GeO_4 nanosheet film is uniformly over the Ni foam. So, it is beneficial to the charge transport and ion diffusion without the necessity of binder blocks, which results in improved charge transfer kinetics.[33] Fig. 6a-6d give typical EDS mapping images of Ge, O, Zn and Mn elements for 7%Mn-Zn_2GeO_4 sample, suggesting the Ge, O, Zn and Mn elements are homogeneously distributing in the EDS mapping of an area in Fig. 6a. The XPS and EDS characterization can reveal information on the chemical components of the 7%Mn-Zn_2GeO_4 sample. According to the EDS and XPS results, the Mn concentration of Mn doped Zn_2GeO_4 samples is 6.9% for the 7%Mn-Zn_2GeO_4 sample.

Fig. 7a-7b gives low-magnification TEM images of Zn_2GeO_4 nanowire array hierarchical nanostructures, showing a uniform length of 2-3 μm and width of 20-30 nm for nanowires. Fig 7c depicts a typical HRTEM lattice image of a Zn_2GeO_4 sample along the [521] zone axis. The marked d-spacings of 0.42 nm and 0.31 nm in the lattice image correspond well with that of (1-31) and (1-1-3) planes of rhombohedral Zn_2GeO_4. The crystal structure is determined according to the FFT pattern in inset of Fig. 7c, suggesting a single-crystalline nature for the synthesized Zn_2GeO_4 nanowire. Low- and high-magnification TEM images in Fig. 8a-8b clearly suggest the interconnected nanosheet hierarchical nanostructures for the 7%Mn-Zn_2GeO_4 sample. A HRTEM lattice image in Fig. 8c reveals an inter-planar spacing of 0.36 nm, corresponding to (220) plane of Zn_2GeO_4. The electron diffraction in Fig. 8d suggests a rhombohedral phase for Mn-doped Zn_2GeO_4 samples. The diffraction rings correspond well with that of (336), (630), (410), (012) planes of Zn_2GeO_4, which is in good agreement with the XRD results.

To investigate the redox reactions of the Mn-doped Zn_2GeO_4 electrode samples, CV curves for the first five cycles of pure Zn_2GeO_4 and 7%Mn-doped Zn_2GeO_4 samples are tested in the voltage window of 0.01-3 V at a scan rate of 0.1 mV s^{-1}. The CV curves of pure Zn_2GeO_4 sample and 7%Mn-Zn_2GeO_4 sample grown on Ni foam are shown in Fig. 9a-9b. In the first cycle, a sharp reduction peak at about 0.55 V can be attributed to the reduction of Zn_2GeO_4 into Zn, Ge, Li_2O and formation of the solid electrolyte interface (SEI), corresponding to Eq. 1.

Another pronounced reduction peak at about 0.15 V can be assigned to the reactions of Li-Zn and Li-Ge, as shown in Eq. 2 and 3.[13,16] In the anodic process, an obvious peak located at 0.5 V is ascribed to the delithiation of Li-Zn and Li-Ge alloys, corresponding to the reverse process of Eq. 2 and 3. The second oxidation peak at about 1.4 V is associated with the reoxidation of Zn and Ge. From the second cycle, the CV curves of Zn_2GeO_4 and Mn-doped Zn_2GeO_4 samples grown on Ni foam are nearly overlapped in the next cycles, indicating Ni foam enhances the cycling stability of the electrode.

Fig 9c-9d shows the 1-5th charge/discharge profiles of the Zn_2GeO_4 nanowire array and 7%Mn-Zn_2GeO_4 nanosheet array at a current density of 100 mA g^{-1} over the potential range 0.01-2.0 V. The discharge curves show a distinct plateau at about 0.75 V, corresponding to the reduction of Zn_2GeO_4 to Zn, Ge, Li_2O and the formation of the solid electrolyte interface (SEI).[13-16] Another plateau at 0.15 V is related to the alloy reaction of Li-Zn and Li-Ge. There exist also two plateaus at 0.5 and 1.4 V in charge process, corresponding to the dealloying reaction and reoxidation of Zn and Ge. The initial discharge and charge capacities of the pure Zn_2GeO_4 nanowire array are 2121 and 888 mA h g^{-1}, corresponding to the columbic efficiency of 41.9%. The capacity loss could mainly result from the irreversible reduction of Zn_2GeO_4 into Ge and Zn, formation of Li_2O and a SEI layer.[13] Interestingly, he first columbic efficiency of the 7%Mn-doped Zn_2GeO_4 interconnected nanosheet array increases to 61.3 %, which is higher than that of Zn_2GeO_4 nanowire array and other metal geramnate samples, such as Zn_2GeO_4-graphene composite (59.6%),[13] amorphous Zn_2GeO_4 (35%),[18] $Ca_2Ge_7O_{16}$ (20%)[20,21]and $BaGe_4O_9$ nanowire (25.6%).[21] The first columbic efficiency of 3%Mn, 5%Mn and 9%Mn-Zn_2GeO_4 samples are 47.4%, 52.2% and 53.8% respectively, which indicates that the morphology and Mn doping can enhance the first columbic efficiency and electrochemical performance of Mn doped Zn_2GeO_4 nanosheet array on Ni foam. Fig. S4 shows the coulombic efficiency of the synthesized samples within the 100 discharge/charge cycles. During the second cycle, the coulombic efficiency of the pristine Zn_2GeO_4 sample is 87.3%. However, the coulombic efficiency of the Mn doped Zn_2GeO_4 samples all reach above 90%, (3%Mn-: 91.9%; 5%Mn: 92.7%; 7%Mn: 93.1%; and 9%Mn-Zn_2GeO_4: 90.9%). The coulombic efficiency of the synthesized samples can all reach 99% after 100 cycles, displaying a good cycling performance.

Fig. 10 shows the resulted Nyquist plots of the AC impedance for the Zn_2GeO_4 sample and Mn-doped Zn_2GeO_4 samples, which are measured at an open circuit voltage state before cycling. The inset in Fig. 10 gives the equivalent circuit model of this cell system. Each plot consists of a semicircle in the high and middle frequency and an inclined line in low frequency region. The high-frequency semicircle corresponds to the contact resistance (R_f) for lithium ion migration through the SEI film (CPE2). The semicircle in the medium-frequency region is attributed to the constant phase element of the electrode-electrolyte interface (CPE1) and charge-transfer

impedance (R_{ct}), and the Warburg impedance (W) is related to lithium ions transfer process in solid electrode materials.[37] Obviously, the Mn-doped Zn_2GeO_4 nanosheet array samples grown on Ni foam have the smaller R_{ct} value than that of pure Zn_2GeO_4 nanowire array sample, indicating Mn-doping in the Zn_2GeO_4 sample could reduce the charge transfer resistance. 7%Mn-Zn_2GeO_4 sample shows the smallest diameter than other sample, which means the 7%Mn-Zn_2GeO_4 sample demonstrates the greatly improved charge transfer kinetics.[5,37]

The lithium ion diffusion coefficient in electrode materials can be calculated from the plots in the low-frequency region according to the following equation: [37,42]

$$Z_{re} = R_{ct} + R_e + \sigma\omega^{-1/2} \quad (6)$$

$$D_{Li} = \frac{R^2T^2}{2A^2n^4F^4C_{Li}^2\sigma^2} \quad (7)$$

Where D is the lithium ion diffusion coefficient, R is the gas constant, T is the absolute temperature, A is the surface area, n is the number of electron (s) per molecule oxidized, F is Faraday's constant, C is the concentration, σ is the Warburg factor, and ω is frequency.[42] Fig. S5 shows the relationship between impendence and the phase angle, demonstrating that the 7%Mn-Zn_2GeO_4 sample displays the smallest Warburg factor, corresponding to the largest lithium ion diffusion coefficient in electrode.[37,42]

Galvanostatic technique is utilized to investigate the cycle performances of Zn_2GeO_4 electrodes in the potential window of 0.01-2.0 V at a current density of 100 mA g^{-1}, as shown in Fig. 11a. It is clearly indicated that Mn-doped Zn_2GeO_4 samples demonstrate an outstanding electrochemical performance. It should be noted that the capacity increase phenomenon of 7%Mn-Zn_2GeO_4 electrode after 50 cycles, is normally observed for metal oxides and is well-documented in the literatures.[13,14,18] Zou et al.[13] reported the phenomenon of capacity increase in Zn_2GeO_4-GO electrode with 12.1 wt% GO. The capacity also continuously increases for hundreds of cycles in amorphous Zn_2GeO_4 sample reported by Yi et al.[18] Though the capacity increase phenomenon exists, the exact underlying mechanism is not very clear. In the case of Mn doped Zn_2GeO_4, the capacity increasing is possibly related to the slow activation process of Zn_2GeO_4 upon lithiation/delithiation process. The factors of Mn doping level, electrical conductivity, and structure morphology may all influence the lithium ion storage performance.[14,18]

After 100 cycles, the 7%Mn-Zn_2GeO_4 sample shows a higher capacity of 1301 mAh g^{-1}, nearly approaching to the theoretical capacity, which is larger than that of previously reported N-doped graphene/Zn_2GeO_4 nanocomposite (1044 mA h g^{-1}),[14] partially crystalline Zn_2GeO_4 nanorod/graphene composites (768 mA h g^{-1}),[16] and Zn_2GeO_4 nanorods (616 mA h g^{-1}).[17] As for the pure Zn_2GeO_4 nanowire sample, it displays a reversible

capacity of 660 mA h g^{-1} at a current density of 100 mA g^{-1} after 100 cycles. Compared with the pristine Zn_2GeO_4 samples reported by other researchers,[13,16] the pristine Zn_2GeO_4 nanowire sample anchored on Ni foam demonstrated the good cycling performance in our investigation. The improved electrochemical performance of the pristine Zn_2GeO_4 nanowire sample anchored Ni foam can be attributed to the Ni foam three dimensional structure. The three dimensional Ni foam acts as a mechanical buffer to relax the volume changes of the Zn_2GeO_4 nanowire generated during Li^+ insertion/extraction, and as a conductive path to enhance the conductivity of the electrode, leading to a high rate capability and better cyclic stability.[4,15] We also test the cycling performance of the pristine Zn_2GeO_4 nanowire sample not on the Ni foam by coating the sample on the copper foil. Fig. S6 shows the cycling and rate performance of the pristine sample not on the Ni foam, displaying a poor cycling capacity of 191 mA h g^{-1} after 100 cycles, which is consistent with the results reported by other researchers.[13,16] This result also demonstrates that 3D Ni foam plays an important role on the performance improvement of this binder-free electrode. Compared with the pure Zn_2GeO_4 sample, 7%Mn-Zn_2GeO_4 nanosheet array hierarchical nanostructures anchored on Ni foam exhibits a higher specific capacity, almost two times higher than that of pure Zn_2GeO_4 sample. We further investigate the electrochemical performance of 9%Mn-Zn_2GeO_4 anode. It is shown that after the Mn doping concentration increases to 9%, the electrochemical performance degrades, the 9% Mn-Zn_2GeO_4 anode displays a 100^{th} cycle specific capacity of 933 mA h g^{-1} at a current density of 100 mA g^{-1}, much lower than that of 7%Mn-Zn_2GeO_4 anode. Our result is consistent with the previous reports. Xu et al.[34] reported the Mn doped V_2O_5 sheet network as electrode for LIBs anode. Their results show that the specific capacity of 5% Mn doped V_2O_5 anode is much higher than that of 10% Mn doped V_2O_5 anode.

The rate capability of Zn_2GeO_4 and Mn-doped Zn_2GeO_4 electrodes is investigated under various current densities of 0.1, 0.2, 0.5, 1.0, and 2.0 A g^{-1}, as shown in Fig. 11b. The Mn-doped Zn_2GeO_4 nanosheet array samples demonstrate a higher rate capability than that of pure Zn_2GeO_4 nanowire array sample. The 7%Mn-doped Zn_2GeO_4 sample can deliver a charge capacity of 1307, 1119, 861, 698 and 500 mA h g^{-1} at current density of 0.1, 0.2, 0.5, 1.0 and 2.0 A g^{-1}, respectively. As the current is set back to 0.1 A g^{-1}, the capacity is able to retain more than 1213 mA h g^{-1}. The result shows that almost 93 % of the capacity at 0.1 A g^{-1} can be recovered after 60 cycles. The pure Zn_2GeO_4 nanowire array sample displays a specific capacity of 725 mA h g^{-1} at the current density of 0.1 A g^{-1} after 10 cycles, 586 mA h g^{-1} at the current density of 0.2 A g^{-1} after 10 cycles, 427 mA h g^{-1} at the current density of 0.5 A g^{-1} after 30 cycles, 303 mA h g^{-1} at the current density of 1.0 A g^{-1} after 40 cycles, 145 mA h g^{-1} at the current density of 2.0 A g^{-1} after 50 cycles. These results demonstrate that Mn-doped Zn_2GeO_4 samples display the higher rate capacity than that of pure Zn_2GeO_4 sample. The specific capacity of 7%Mn-Zn_2GeO_4 is

approximately about 3.4 times higher than that of pure Zn_2GeO_4 sample at the current density of 2.0 A g^{-1}. This could be a confirmation of the exceptional capability of Mn-doped Zn_2GeO_4 electrode to keep its integrity not only a long number of cycles but also at high rates.

The greatly improved electrochemical performance of the Mn-doped Zn_2GeO_4 electrode can be attributed to the synergistic effects between Zn_2GeO_4 hierarchical nanostructure and 3D Ni foam porous structure, the improvement of charge transport kinetics at the interface between the electrode and electrolyte resulted from the Mn doping. (1) Mn doped Zn_2GeO_4 nanosheet sample shows a better structure stability than that of pure Zn_2GeO_4 nanowire sample. Fig. S7 shows the morphology of the pure Zn_2GeO_4 nanowire samples after 10 cycles, indicating that the structure of Zn_2GeO_4 nanowire is not easy retained because of the pulverization and cracking effect. Fig. S8 shows the SEM images of the nanosheets at both lithiated state (Fig. S 8a-8b) and delithiated state (Fig. S 8c-8d) after 100 cycles at the current density of 100 mA g^{-1}. The high magnification SEM image shows that the thickness of the nanosheets increases from 15 nm for nanosheets before cycling (Fig. S2.) to about 70-80 nm for nanosheet at lithiated state, which may be attributed to the SEI formation. The thickness of the nanosheets of about 30-40 nm at delithiated state is still thicker than that before cycling. However, importantly, the nanosheet electrodes can still maintain its network as well as interconnected porous structures after charging the cell back, suggesting that it has a high structural stability for the nanosheet array hierarchical nanostructures. (2) It is shown that the Mn-doped Zn_2GeO_4 samples display typically hierarchical nanosheet interconnected arrays anchored on porous Ni foam. It is believed that the space between the interconnected Mn-doped Zn_2GeO_4 nanosheet arrays (not the nanosheet self) plays a very important role in relaxing the volume changes. The space between Zn_2GeO_4 nanosheet array structure can supply enough space to buffer the volume change caused by electrochemical reaction.[40] On the other hand, the three dimensional Ni foam possesses a larger surface area, corresponding to the larger contact area between Ni foam collector and Zn_2GeO_4 active materials. The large contact area can decrease the stresses caused by volume changes during litigation/delithiation process of the active Zn_2GeO_4 materials on unit area. So the three dimensional Ni foam collector can further accommodate the volume expansion of active materials during discharge/charge process.[4,15,41] (3) The 3D Ni foam functions as a substrate not only to buffer the volume change, but also enhance the conductivity of the electrode, providing a highway for fast electron transport to the current collector, efficiently reducing ohmic polarization, leading to a high rate capability and better cyclic stability. The resulted Nyquist plots of the AC impedance shows that Mn cationic doping further improves electrical conductivity and charge transfer ability and thus enhances the electrochemical performance of Zn_2GeO_4 materials. The decrease of charge transfer resistance is beneficial for obtaining improved chemical performance, leading to a large specific capacity and perfect cyclic performance. (4) The incorporation of Mn into Zn_2GeO_4

induces a great microstructure evolution from nanowire array hierarchical nanostructures for pure Zn_2GeO_4 sample to Mn-doped Zn_2GeO_4 nanosheet array hierarchical nanostructures, leading a higher interaction area between active materials and electrolyte (Fig. 12). The distinctive structure of Mn-doped Zn_2GeO_4 nanosheet array hierarchical nanostructrues grown on Ni foam increase the initial coulombic efficiency and enhances the lithium ion storage capacity.

4. Conclusions

We developed a facile synthesis route to prepare three dimensional Zn_2GeO_4 hierarchical nanostructrures on Ni foam via a simple one-step hydrothermal method on a large scale. It is found that incorporation of Mn into Zn_2GeO_4 is an effective method to modulate microstructure and electrochemical lithium storage performance. The incorporation of Mn into Zn_2GeO_4 induces a great microstructure evolution from nanowire structure for pure Zn_2GeO_4 sample to Mn-doped Zn_2GeO_4 nanosheet sample on Ni foam. The Zn_2GeO_4 nanowire array and 7%Mn-Zn_2GeO_4 nanosheet array hierarchical nanostructrues grown on the Ni foam exhibit a high reversible capacity of 660 and 1301 mA h g^{-1} respectively, displaying excellent cycling stability. At a high rate of 2.0 A g^{-1}, the discharge capacity of 7%Mn-Zn_2GeO_4 nanosheet material remains at 500 mA h g^{-1}, displaying a good rate capability. The great enhancement of the electrochemical lithium storage performance can be attributed to three-dimensional interconnected conductive channels composed of the Ni foam, which not only serves as the current collector but also buffers the volume change of the active material upon cycling. Additionally, the Mn doping can greatly improve charge transport kinetics at the interface between the electrode and electrolyte.

ACKNOWLEDGEMENTS

We acknowledge support from the Sate Key Program of National Natural Science of China (No.: 51532005), National Nature Science Foundation of China (No.: 51272137, 51472148), and the Tai Shan Scholar Foundation of Shandong Province.

REFERENCES

1 M. Armand and J. M. Tarascon, *Nature*, 2008, **451**, 652-657.

2 B. Dunn, H. Kamath and J. M. Tarascon, *Science*, 2011, **334**, 928-935.

3 M. V. Reddy, G. V. Subba Rao and B. V. R. Chowdari, *Chem. Rev.*, 2013, **113**, 5364-5457.

4 W. Yang, G. Cheng, C. Dong, Q. Bai, X. Chen, Z. Peng and Z. Zhang, *J. Mater. Chem. A*, 2014, **2**, 20022-20029.

5 Q. Li, L. Yin, Z. Li, X. Wang, Y. Qi and J. Ma, *ACS Appl. Mater. Interfaces*, 2013, **5**, 10975-10984.

6 H. Wu and Y. Cui, *Nano Today*, 2012, **7**, 414-429.

7 Y. Hwa, C. M. Park, S. Yoon and H. Sohn, *Electrochimica Acta*, 2010, **55**, 3324-3329.

8 K. H. Seng, M. Park, Z. Guo, H. K. Liu and J. Cho, *Nano Lett*., 2013, **13**, 1230-1236.

9 D. Lv, M. L. Gordin, R. Yi, T. Xu, J. Song, Y. Jiang, D. Choi and D. Wang, *Adv. Funct. Mater.*, 2014, **24**, 1059-1066.

10 D. Xue, S. Xin, Y. Yan, K. Jiang, Y. Yin, Y. Guo and L. Wan, *J. Am. Chem. Soc.*, 2012, **134**, 2512-2515.

11 M. Liu, X. Ma, L. Gan, Z. Xu, D. Zhu and L. Chen, *J. Mater. Chem. A*, 2014, 2, 17107-17114.

12 G. Derrien, J. Hassoun, S. Panero and B. Scrosati, *Adv. Mater.*, 2007, **19**, 2336-2340.

13 F. Zou, X. Hu, L. Qie, Y. Jiang, X. Xiong, Y. Qiao and Y. Huang, *Nanoscale*, 2014, **6**, 924-930.

14 F. Zou, X. Hu, Y. Sun, W. Luo, F. Xia, L. Qie, Y. Jiang and Y. Huang, *Chem. Eur. J.*, 2013, **19**, 6027-6033.

15 W. Li, X. Wang, B. Liu, J. Xu, B. Liang, T. Luo, S. Luo, D. Chen and G. Shen, *Nanoscale*, 2013, **5**, 10291-10299.

16 R. Wang, S. Wu, Y. Lv and Z. Lin, *Langmuir*, 2014, **30**, 8215-8220.

17 J. K. Feng, M. O. Lai and L. Lu, *Electrochem. Commun.*, 2011, **13**. 287-289.

18 R. Yi, J. Feng, D. Lv, M. L. Gordina, S. Chena, D. Choi and D. Wang, *Nano Energy*, 2013, **2**, 498-504.

19 W. Li, X. Wang, B. Liu, S. Luo, Z. Liu, X. Hou, Q. Xiang, D. Chen and G. Shen, *Chem. Eur. J.*, 2013, **19**, 8650-8656.

20 T. Lv, X. Li and J. Ma, *RSC Adv*., 2014, **4**, 49942-49945.

21 W. Li, Y. Yin, S. Xin, W. Song and Y. Guo, *Energy Environ. Sci.*, 2012, **5**, 8007-8013.

22 S. Jin and C. Wang, *Nano Energy* 2014 **3**, 63-71.

23 S. Wu, R. Wang, Z. Wang and Z. Lin, *Nanoscale*, 2014, **6**, 8350-8358.

24 C. H. Kim, Y. S. Jung, K. T. Lee, J. H. Ku and S. M. Oh, *Electrochimica Acta*, 2009, **54**, 4371-4377.

25 F. Zhang, R. Zhang, Z. Zhang, H. Wang, J. Feng, S. Xiong and Y. Qian, *Electrochimica Acta*, 2014, **150**, 211-217.

26 T. Wang, Q. Liu, G. Li, K. Xu, R. Zou and J. Hu, *CrystEngComm*, 2014, **16**, 3222-3227.

27 W. Zhao, C. Zhang, Y. Shi, R. Wu and B. Zhang, *Dalton Trans.*, 2015, **44**, 75-82.

28 S. Takeshita, J. Honda, T. Isobe, T. Sawayama and S. Niikura, *Crystal Growth & Design*, 2010, **10**, 4494-4500.

29 Q. Liu, Y. Zhou, J. Kou, X. Chen, Z. Tian, J. Gao, S. Yan and Z. Zou, *J. Am. Chem. Soc.* 2010, **132**, 14385-14387.

30 J. Liu, G. Zhang, J. C. Yu and Y. Guo, *Dalton Trans.*, 2013, **42**, 5092-5099.

31 I. Kovalenko, B. Zdyrko, A. Magasinski, B. Hertzberg, Z. Milicev, R. Burtovyy, I. Luzinov and G. Yushin, *Science*, 2011, **334**, 75-79.

32 Y. Cao, W. Li, K. Xu, Y. Zhang, T. Ji, R. Zou, J. Yang, Z. Qin and J. Hu, *J. Mater. Chem. A*, 2014, **2**, 20723-20728.

33 G. Li, W. Li, K. Xu, R. Zou, Z. Chen and J. Hu, *J. Mater. Chem. A,* 2014, **2**, 7738-7741.

34 Y. Xu, M. Dunwell, L. Fei, E. Fu, Q. Lin, B. Patterson, B. Yuan, S. Deng, P. Anderson, H. Luo and G. Zou, *ACS Appl. Mater. Interfaces*, 2014, **6**, 20408-20413.

35 H. Wang, B. Wang, J. Meng, J. Wang and Q. Jiang, *J. Mater. Chem. A*, 2015, **3**, 1023-1030.

36 B. Liu, X. Zhao, Y. Xiao and M. Cao, *J. Mater. Chem. A*, 2014, **2**, 3338-3343.

37 S. Takeshita, J. Honda, T. Isobe, T. Sawayama and S. Niikura, *J. Solid State Chem.*, 2012, **189**, 112-116.
38 A. A. Audi and P. M. A. Sherwood, *Surf. Inter. Anal.*, 2002, **33**, 274-282.
39 Y. Sun, X. Hu, W. Luo, F. Xia and Y. Huang, *Adv. Funct. Mater.*, 2013, **23**, 2436-2444.
40 X. Wang, L. Qiao, X. Sun, X. Li, D. Hu, Q. Zhang and D. He, *J. Mater. Chem. A*, 2013, **1**, 4173-4176.
41 X. Li, Z. Yang, Y. Fu, L. Qiao, D. Li, H. Yue and D. He, *ACS nano*, 2015, **9**, 1858-1867.
42 G. Q. Liu, H. T. Kuo, R. S. Liu, C. H. Shen, D. S. Shy, X. K. Xing and J. M. Chen, *J. Alloys Compd.* 2010, **496**, 512-516.

Figure Captions

Fig. 1. XRD patterns of the samples. (a) pure Zn_2GeO_4sample, (b) 7%Mn-Zn_2GeO_4 sample, (c) and (d) magnified (220) and (410) peak of Zn_2GeO_4 and 7%Mn-Zn_2GeO_4 samples.

Fig. 2. XPS spectra of 7%Mn-Zn_2GeO_4 nanosheet sample. (a) Survey spectrum, (b) Ge 3d, (c) Zn 2p, (d) Mn 2p.

Fig. 3. FESEM images of pure Zn_2GeO_4 samples. (a) Low magnification, and (b-d) high magnification.

Fig. 4. (a-c) FESEM images of 3%Mn-Zn_2GeO_4 hierarchical nanostructured samples grown on Ni foam. (d) FESEM images of 5%Mn-Zn_2GeO_4 hierarchical nanostructures anchored on porous Ni foam.

Fig. 5. FESEM images of 7%Mn-Zn_2GeO_4 nanosheet array hierarchical nanostructures anchored on porous Ni foam. (a) low magnification, (b-d) high magnification.

Fig. 6. Elemental mapping images of 7%Mn-Zn_2GeO_4 nanosheet samples. (a) Ge, (b) O, (c) Zn and (d) Mn. The inset in (a) is corresponding SEM image.

Fig. 7. TEM images of pure Zn_2GeO_4 sample. (a-b) low magnification TEM images, (c) High-resolution TEM image of the Zn_2GeO_4 nanowire. The inset right upper side is corresponding FFT pattern of the pure Zn_2GeO_4 sample.

Fig. 8. TEM images of 7%Mn-Zn_2GeO_4 sample, (a) and (b) low magnification TEM images, (c) High-resolution TEM image, (d) SAED patterns of synthesized sample.

Fig. 9. Cyclic voltammetry (CV) curves of the first five cycles for (a) pure Zn_2GeO_4 sample, (b) 7%Mn-Zn_2GeO_4 sample electrode scan rate of 0.1 mV s^{-1} between 0.01 and 3.0 V. Discharge-charge profiles of (c) pure Zn_2GeO_4 sample and (d) 7%Mn-Zn_2GeO_4 electrodes at a current density of 100 mA g^{-1} in the voltage range 0.01-2.00 V versus Li^+/Li.

Fig. 10. Nyquist plots of the AC impedance for synthesized samples. The inset is the equivalent circuit model of this cell system.

Fig. 11. (a) Cyclic performance and (b) rate performances of the synthesized samples.

Fig 12. Discharge-charge mechanism of the synthesized Zn_2GeO_4 samples anchored on porous Ni foam.

Fig. 1

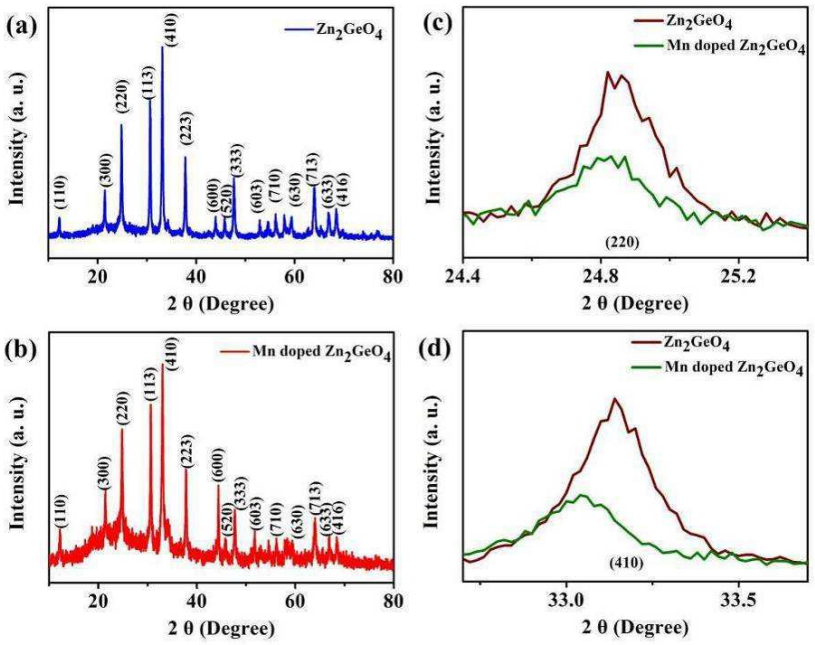

Fig. 2

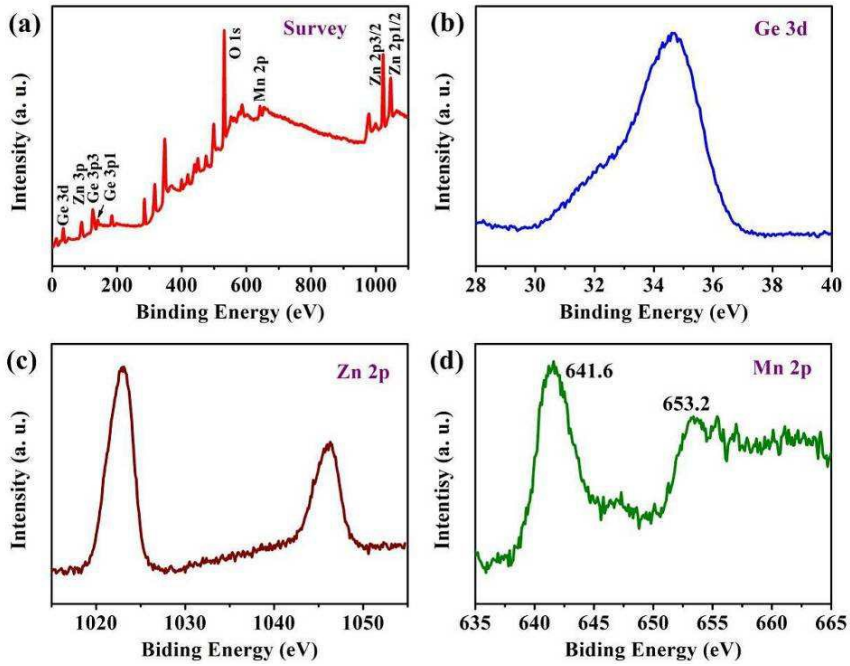

Fig. 3

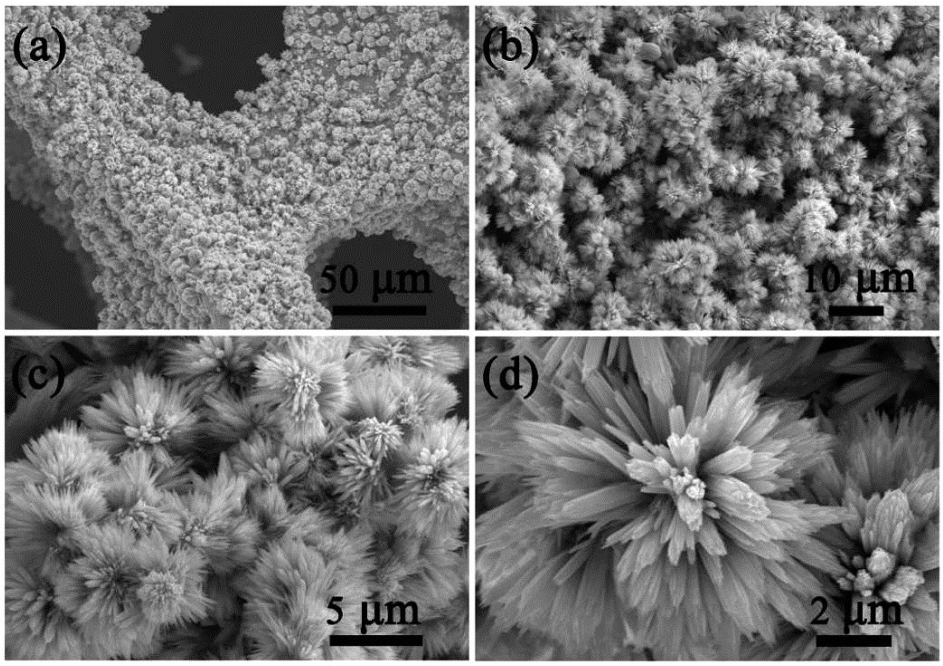

Fig. 4

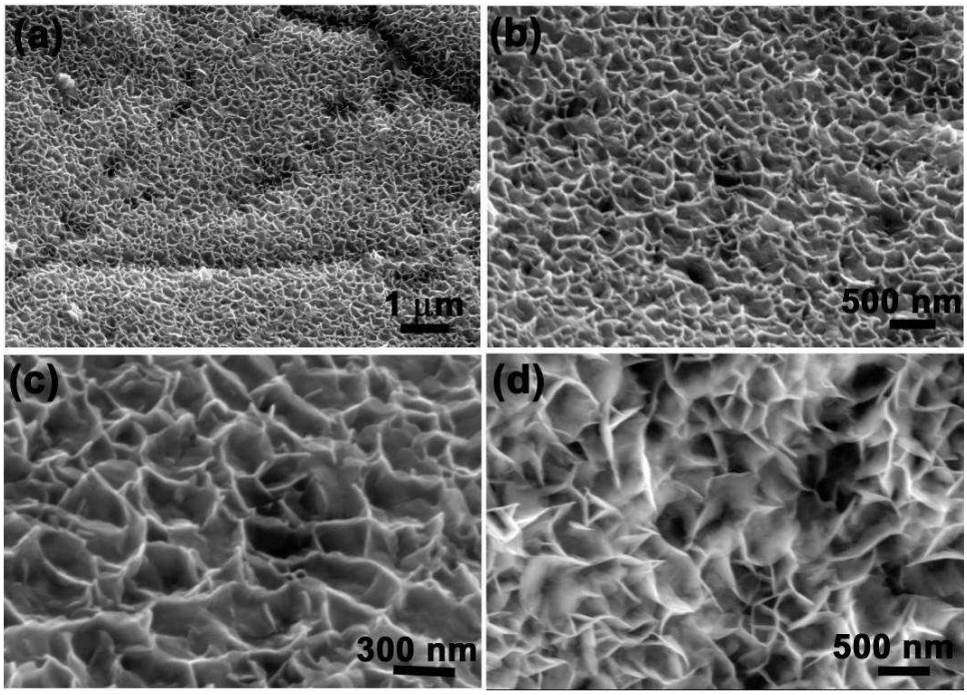

Fig. 5

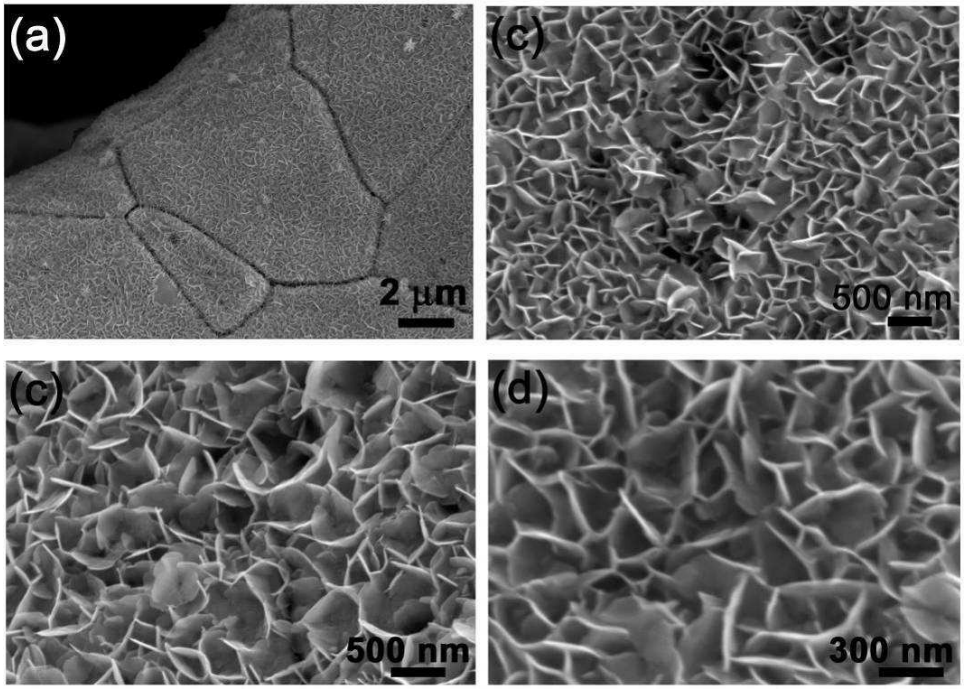

Fig. 6

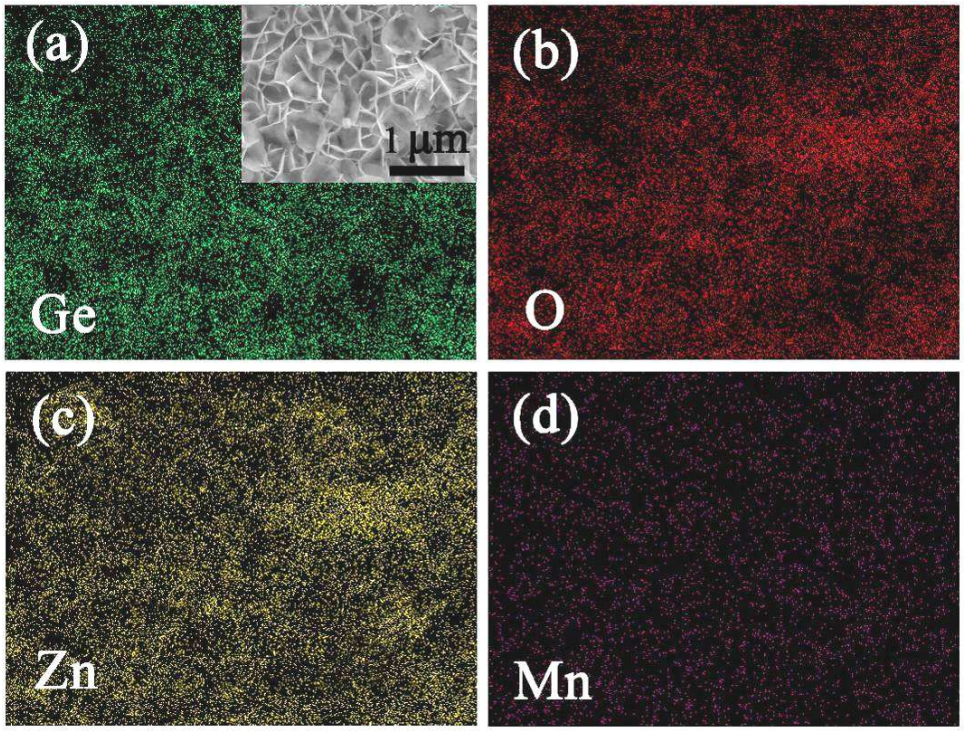

Fig. 7

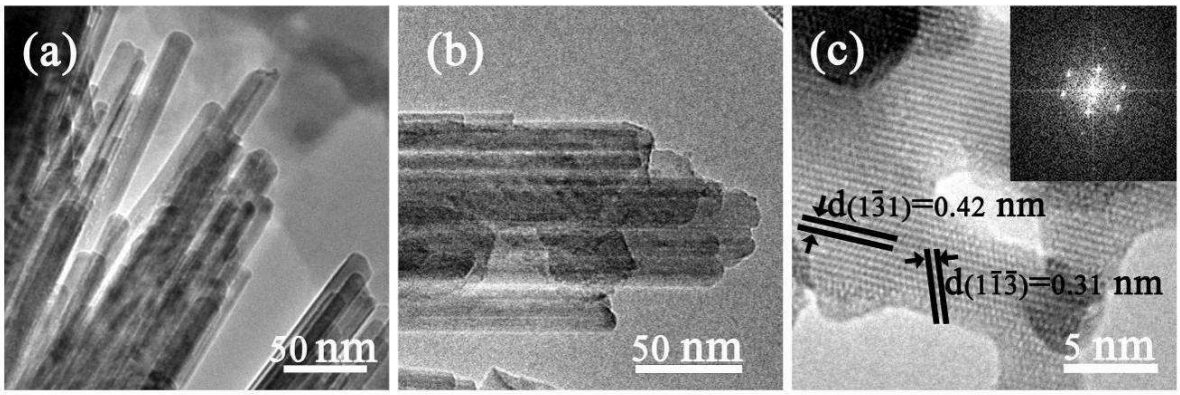

Fig. 8

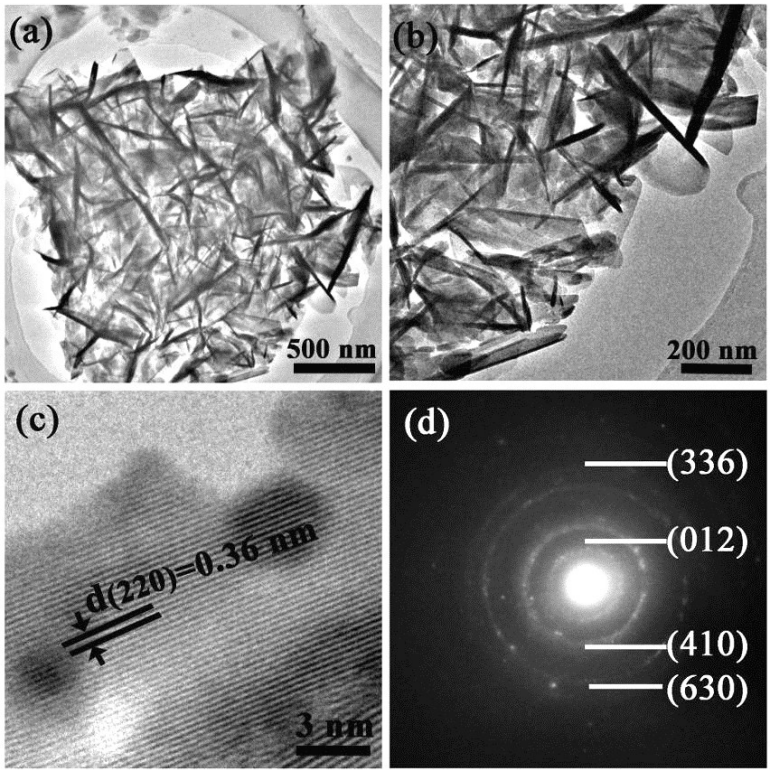

Fig. 9

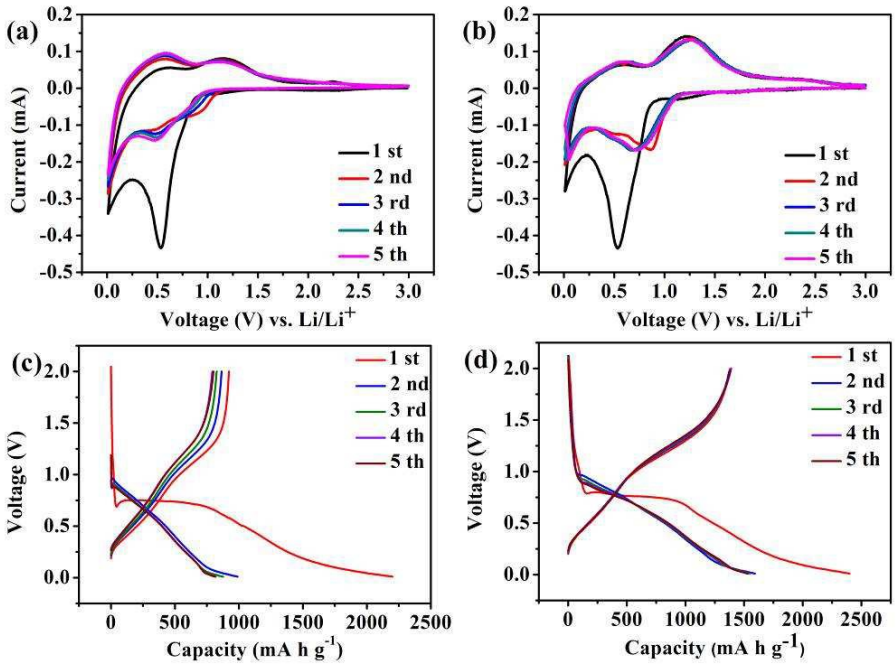

Fig. 10

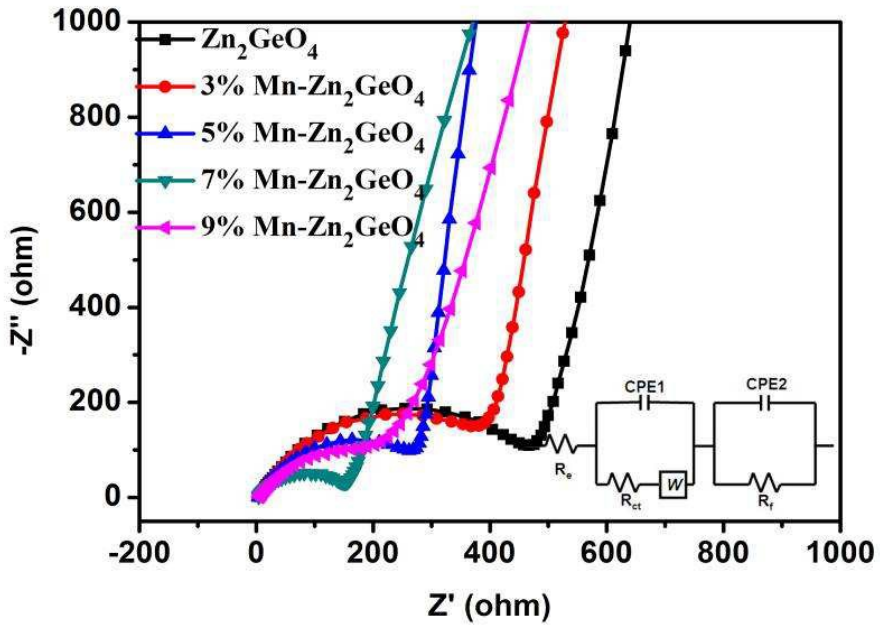

Fig. 11

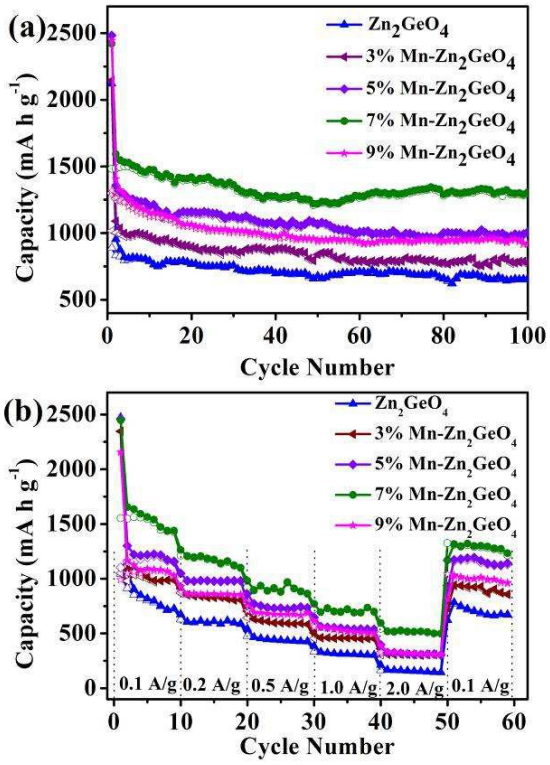

Fig. 12

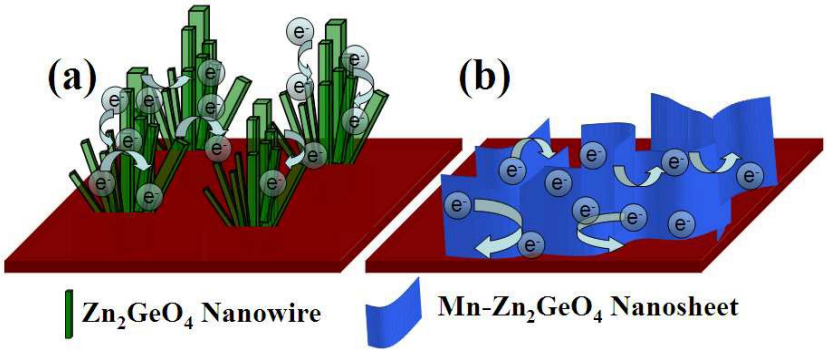

TOC

Mn doping effectively induces a great microstructure evolution from nanowire array for pure Zn_2GeO_4 to nanosheet array for Mn-doped Zn_2GeO_4 samples anchored on Ni foam, and enhanced lithium ion storage performance.